Journal of Sound and Vibration (2002) **255**(5), 819–848
doi:10.1006/jsvi.2001.4188, available online at http://www.idealibrary.com on IDEAL®

STATISTICAL PROPERTIES OF RANDOM SPARSE ARRAYS

H. KOOK

School of Mechanical and Automotive Engineering, Kookmin University, 861-1, *Chongnung-dong, Songbuk-gu, Seoul* 136-702, *Korea. E-mail*: *kook@kookmin.ac.kr*

AND

P. DAVIES AND J. S. BOLTON

Ray W. Herrick Laboratories, School of Mechanical Engineering, Purdue University, West Lafayette, IN 47907-1077, *U.S.A.*

(*Received* 17 *July* 2000, *and in final form* 3 *December* 2001)

Theoretical models that can be used to predict the range of mainlobe widths and the probability distribution of the peak sidelobe levels of two-dimensionally sparse arrays are presented here. The arrays are considered to comprise microphones that are randomly positioned on a segmented grid of a given size. First, approximate expressions for the mean and variance of the squared magnitude of the aperture smoothing function are formulated for the random arrays considered in the present study. By using the variance function, the mean value and the lower end of the range i.e., the first 1 per cent of the mainlobe width distribution, can be predicted with reasonable accuracy. To predict the probability distribution of the peak sidelobe levels, distributions of levels were modelled by using a Weibull distribution at each peak in the sidelobe region of the mean squared magnitude of the aperture smoothing function. The two parameters of the Weibull distribution were estimated from the means and variances of the levels at the corresponding locations. Next, the probability distribution of the peak sidelobe levels were identified by following a procedure in which the peak sideload level was determined as the maximum among a finite number of independent random sidelobe levels. It was found that the model obtained from that approach predicts the probability density function of the peak sidelobe level distribution reasonably well for the various combinations of the two different numbers of microphones and the various grid sizes tested in the present study. The application of these models to the design of random, sparse arrays having specified performance levels is discussed.

1. INTRODUCTION

As described in a previous article [1], it is possible to use a stationary array of microphones to identify the locations and strengths of the noise sources that contribute to an accelerating vehicle's sideline noise level. An unusual feature of that method is that it can be used in the case when the source vehicle moves at a non-constant velocity: during a standard vehicle passby test, for example. In such a test, the position of the vehicle is tracked continuously by using a radar transducer (which measures the vehicle's velocity) and a photoelectric sensor is used to identify the absolute position of the vehicle at one time. From the vehicle's position as a function of time, propagation distances from assumed source locations on a restoration plane (attached to and moving with the side plane of the vehicle) to the

0022-460X/02/$35.00

stationary array microphones are calculated. Based on those propagation distances, each microphone signal is de-Dopplerized and corrected for the amplitude attenuation resulting from spherical spreading. The processed microphone signals can then be focused on a sequence of locations on the restoration plane to yield the spatial distribution of source strengths at any vehicle position during the passby.

A microphone array to be used for this purpose must satisfy various, sometimes conflicting, requirements. For example, the microphones must be spaced sufficiently closely to avoid spatial aliasing while at the same time the total array aperture must be large enough to allow typical sources to be resolved accurately. To satisfy these requirements by using a fully populated array suggests the need for an unrealistically large number of microphones, potentially in the thousands.

However, it is known that the conditions listed above may be met by using so-called sparse arrays in which microphones are not placed at all of an aperture's underlying grid locations. In the case of linear sparse arrays, it is known that mainlobe width is essentially the same as that of the equivalent fully populated array so long as the aperture size of the sparse array is the same as that of the fully populated array on the underlying grid [2]. Since the spatial anti-aliasing performance of an array is determined by the minimum spacing in its co-array (i.e., the autocorrelation of the array configuration), sparse arrays possess the same degree of anti-aliasing capability as that of the fully populated array on the underlying grid. However, it is known that the peak sidelobe levels of sparse arrays tend to be higher than those of equivalent fully populated arrays. The peak sidelobe level is related to the noise rejection capability of an array and it is usually an important factor by which the performance for an array configuration is assessed. Given that the aperture size and the number of sensors in a linear sparse array are fixed (i.e., that there are sensors placed at both ends of the underlying grid), a broad range of peak sidelobe levels is possible depending on the precise details of the array configuration. Sidelobe levels can be controlled to some extent by applying spatial windows to the array output. However, the possibility of applying spatial windows to reduce the peak sidelobe levels has been excluded in the present study since the weighting factors for each microphone are assumed to be related to the propagation distances from each point of interest on the restoration plane to each microphone [1].

Note that the co-array of an array represents the number of occurrences of each baseline within the array (the baseline is defined as the distance between a pair of sensors in an array configuration). For an M-sensor array, the maximum number of possible baselines is ${}_M\mathrm{C}_2 = M(M-1)/2$. It is usually the case that sparse arrays feature redundant baselines (i.e., multiple appearances of the same baseline) and lack certain other baselines. The absence of a particular baseline in an array configuration of course means that the incident spatio-temporal sound pressure field cannot be sampled at that baseline. Two methods focusing on the redundancy of an array have been used to design linear arrays having equi-spaced, linear grids: the two methods results in either minimum redundant or non-redundant linear arrays. The design of minimum redundant linear arrays is described by Moffet [3], and by Panayirci and Chen [4]. In the case of a minimum redundant array, the number of redundancies in the co-array is minimized subject to the restriction that there should be no "holes", or zero correlation values, within the array's co-array. Non-redundant linear arrays are described by Vertatschitsch and Haykin [5]: their co-arrays have only zero or unit correlation values (except at zero lag). While a non-redundant array usually yields the largest aperture amongst the possible array types given a fixed number of sensors, the "holes" in the co-array result in sidelobe levels that are likely to be higher than those resulting from the use of a minimum redundant array. The benefit of minimum redundant and non-redundant arrays given a certain number of sensors

is that they result in a relatively large aperture size without unnecessary loss in baselines, thus allowing good spatial resolution (i.e., small mainlobe width) to be obtained. However, given the maximum aperture size and the available number of sensors, the question is: Are either minimum redundant or non-redundant sparse arrays optimal in the sense that they yield the smallest peak sidelobe level amongst all possible sparse arrays that extend over the same aperture size? The work described in the present article was performed in part to address this concern.

The linear array design methods described above cannot be easily extended to the case of two-dimensional sparse arrays. Indeed, it is not even easy to define such an array's "aperture size". There have been relatively few publications related to the design of two-dimensional arrays. One approach to designing two-dimensional arrays was suggested by Klemperer [6]. In his method, non-redundant arrays were generated based on a six-sensor array of zero redundancy to which three sensors at a time were added axisymmetrically on a triangular grid. Among the non-redundant arrays generated, the best array configuration was selected based on the criteria of "compactness" and large "core number", the latter being defined as the total number of baselines in the central portion of the co-array within a limiting circle in which just a small proportion (5–10 per cent) of holes was allowed. However, this method cannot be used to design non-axisymmetrical arrays (for instance, rectangular arrays) in applications where such arrays are preferred. Klemperer's method represents an extension to two dimensions of the philosophy that the array having the smallest number of redundancies will be the best amongst the possible array configurations that could be constructed on the underlying grid.

Another two-dimensional array design method involves the generation of arrays in which sensors are positioned randomly within a given aperture region. The positioning of sensors in a random fashion helps to avoid the periodicity inherent in non-random arrangements, thus possibly flattening the co-array values. Random arrays are essentially extreme versions of non-redundant arrays when a large enough number of sensors are involved. However, to justify the use of array design methods based on minimizing the number of redundancies, it should first be demonstrated that an array having a small number of redundancies generally yields small peak sidelobe levels. To-date, that connection does not appear to have been demonstrated. For example, the correlation between the number of redundancies and the peak sidelobe level of a set of 2000 array configurations generated by randomly placing 16 microphones on a 12×12 grid with a grid spacing of 1/11 m in both the x and z directions (i.e., in the horizontal and vertical directions respectively) is shown in Figure 1 (the procedure used in these calculations will be described in later sections of this article). Even though some degree of correlation can be observed in the data shown in Figure 1, it can also be seen that there is a large variation in peak sidelobe level for a given number of redundancies. Furthermore, since some of the random array configurations possessing relatively low peak sidelobe levels could have relatively large mainlobe widths, it does not seem safe to rely solely on the number of redundancies to identify a good array configuration.

Note that arrays generated by deterministic design methods, e.g., crossed arrays [7] and elliptically spiral array [2], are all subsets of random sparse arrays so long as they share the same underlying grid. Therefore, it might be considered wise to allow an optimal array (satisfying both the mainlobe width and the peak sidelobe requirements) to emerge from an exhaustive search of a population of random arrays without imposing a particular array shape *ab initio*.

In practice, however, the specification of two-digit numbers of grid points in both horizontal and vertical directions (for example, 80×40) in a rectangular aperture to be populated sparsely by a manageable number of sensors (for example, 64) would yield a very

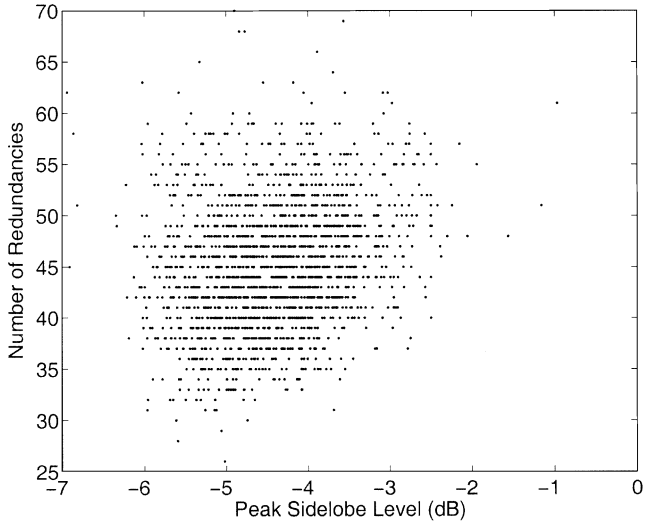

Figure 1. Correlation between the number of redundancies and the peak sidelobe level for 2000 randomly generated 16-microphone array configurations with a 12×12 grid size and 1/11 m grid spacing in the x and z directions.

large number of possible array configurations. As a result, the subset of arrays that can be tested in a reasonable period of time generally represents only a small fraction of the total set of possible arrays. Therefore, it would be of benefit if, when determining the number of sensors and the grid size to be used in a particular application, the ranges of mainlobe widths and peak sidelobe levels of various classes or random array configurations could be estimated before starting a time-consuming search process. Lo [8] developed an approximate method of determining the critical number of sensors required to generate with a good chance of success a random linear array having a specified peak sidelobe level. Lo's approximate method is based on a statistical approach and is asymptotically valid for large numbers of sensors (in his study, cases where the number of sensors was greater than 100 were considered).

In the present article, a similar tool, which can be used even when the number of microphones is relatively small, is described. The model presented in the present study can be used to predict the range of the distributions of the mainlobe widths and the probability distributions of the peak sidelobe levels of randomly generated two-dimensional arrays given the grid size and the number of microphones to be positioned on the grid. In principle, the computationally efficient method presented here can be used to predict the smallest possible mainlobe width and the lowest possible peak sidelobe levels obtained by testing a reasonably small fraction of the total set of possible arrays. Thus, one can use the tools described here to choose an appropriate grid size and spacing given a specified number of sensors before a time consuming, exhaustive search is performed. Alternatively, these tools can be used to estimate the minimum number of sensors that must be used to meet specified requirements for peak sidelobe level, mainlobe width and anti-aliasing performance.

Note finally that it is certainly possible that an array carefully designed according to some specified criteria (shape, for example) might perform better than the best of a finite subset of all possible randomly generated array configurations in terms of peak sidelobe level and mainlobe width. However, it is generally not an easy task to design an array as the number of microphones increases. Even when one attempts to design an array configuration according to some set of arbitrary criteria, the tools that are described in the

present article can be used to establish a standard against which the peak sidelobe levels and the mainlobe width of those array configurations can be compared. As a benchmarking study, the problem of placing 16 and 64 microphones within different-sized, square apertures is also considered here.

2. RANDOM ARRAY GENERATION WITH A SEGMENTING SCHEME

2.1. GRID SPACING

Given a specified aperture in the x–z plane, the fundamental grid spacing in the x and z directions (e.g., in the horizontal and vertical directions respectively) is determined by the spatial anti-aliasing capability required in a specific application. In vehicle passby applications, for example, the fundamental grid spacing is determined by the frequency range of interest and the maximum incidence angle from the vehicle noise sources to the center of the array. Standard motor vehicle passby test procedures are described in ISO 362-1981. In the present work, it was assumed that it is desired to identify the source locations and strengths over a vertical plane (i.e., the x–z plane) extending from -10 to 10 m from the center of the array and horizontally separated from the array: see Figure 2. In that case, the maximum incidence angle occurs when the vehicle is either at the entrance or exit of the test section as depicted in Figure 2. The maximum angle would occur at the entrance side of the array plane when the source is at the exit edge of the noise source plane (or equivalently, at the exit side of the array plane when the source is at the entrance edge of the noise source plane). To avoid spatial aliasing, it is required that there be at least two

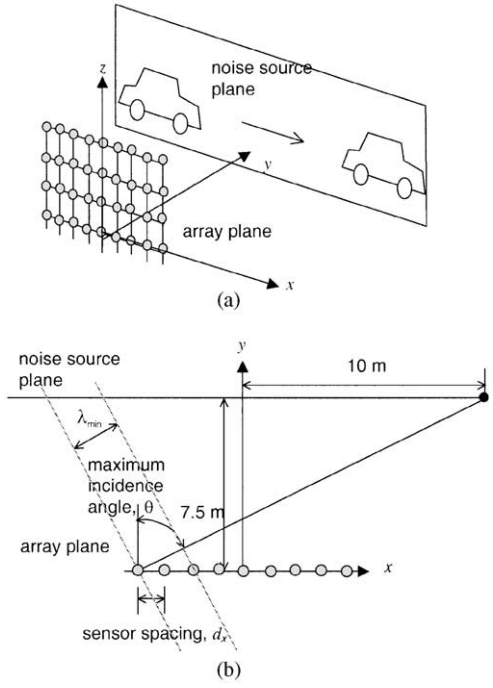

Figure 2. Determination of maximum allowable sensor spacing in the x direction (the direction of vehicle movement): (a) isometric view; (b) top view.

sensor spacings, $2d$, within one spatial cycle of the sound field in the x direction. Therefore, the maximum sensor spacing, d_x, that is allowed in the x direction can be calculated as

$$d_x = \frac{c}{2 f_{max} \sin\theta}, \tag{1}$$

where c is the sound speed and f_{max} is the highest frequency that contributes significantly to the sound field incident on the array. Here, for instance, when f_{max} is 2 kHz, d_x is calculated to be approximately 0·11 m. The present analysis is based on the existence of plane phase planes (the far field source case). However in reality, the noise sources on the restoration plane (the side plane of the vehicle) lie within the "near field" of the microphone array, i.e., spherical spreading effects are significant. An analysis performed assuming spherical phase surfaces would result in a decrease in the allowable sensor spacing in the x direction; an exact analysis would require a knowledge of the microphone positions *a priori*. Therefore, the sensor spacing in the x direction should be selected so that it is smaller than the value calculated above, and the appropriateness of the spacing should be checked after the array design is finalized.

2.2. SEGMENTING SCHEMES

Once the spacing of the underlying regular grid is determined, all the sparse arrays defined on the same underlying grid share the same spatial aliasing characteristics except in the case of sparse arrays in which microphones happen to be placed at integer multiples of the underlying grid spacing (i.e., where the smallest actual microphone spacing is an integer multiple of the nominal grid spacing). The mainlobe width and the peak sidelobe level of a sparse array then depend on the aperture size and the way the microphones are disposed on the grid points.

The mainlobe width, in particular, is strongly related to the aperture size of an array configuration (that relation will be discussed in detail in section 3.2). The aperture sizes of random arrays, and thus the mainlobe width, can to some extent be controlled by specifying the size of the underlying grid. However, when sensors are positioned randomly on the grid, sensors can clump together in a small region thus yielding a smaller effective aperture size than is suggested by the nominal grid size. To make sure that the sensors are spatially well distributed after an appropriate grid size is fixed, schemes based on segmenting the whole aperture into smaller subsections were considered in the present study.

In a segmenting procedure, sensors are first grouped on a segment-by-segment basis, and each group of sensors is then positioned randomly within each subsection as in the random array design method. Moebs [9] first used a segmenting scheme when designing a 16-microphone array in order to resolve the clumping problem. In this case, he segmented a rectangular aperture of size 3 m × 1·8 m (a 16 × 10 grid size) into 3 × 3 subsections of equal width and height. In his method, one microphone was always positioned at the center of the array's aperture and the rest of the microphones were positioned randomly within the various subsections.

Three segmenting schemes for a square, 12 × 12 grid are illustrated in Figure 3. Since the width and height of the 12 × 12 grid was specified to be 1 m × 1 m, the grid spacing, d_x and d_z, was approximately 0·09 cm. To study the effects of segmenting the baseline grid into uniform subsections, the baseline aperture (denoted segmenting scheme 1) shown in Figure 3(a) was uniformly divided into 2 × 2 subsections and 4 × 4 subsections as shown in Figure 3(b) and 3(c); the latter arrays will be referred to as resulting from the application of segmenting schemes 2 and 3 respectively. As the number of uniform subsections increases,

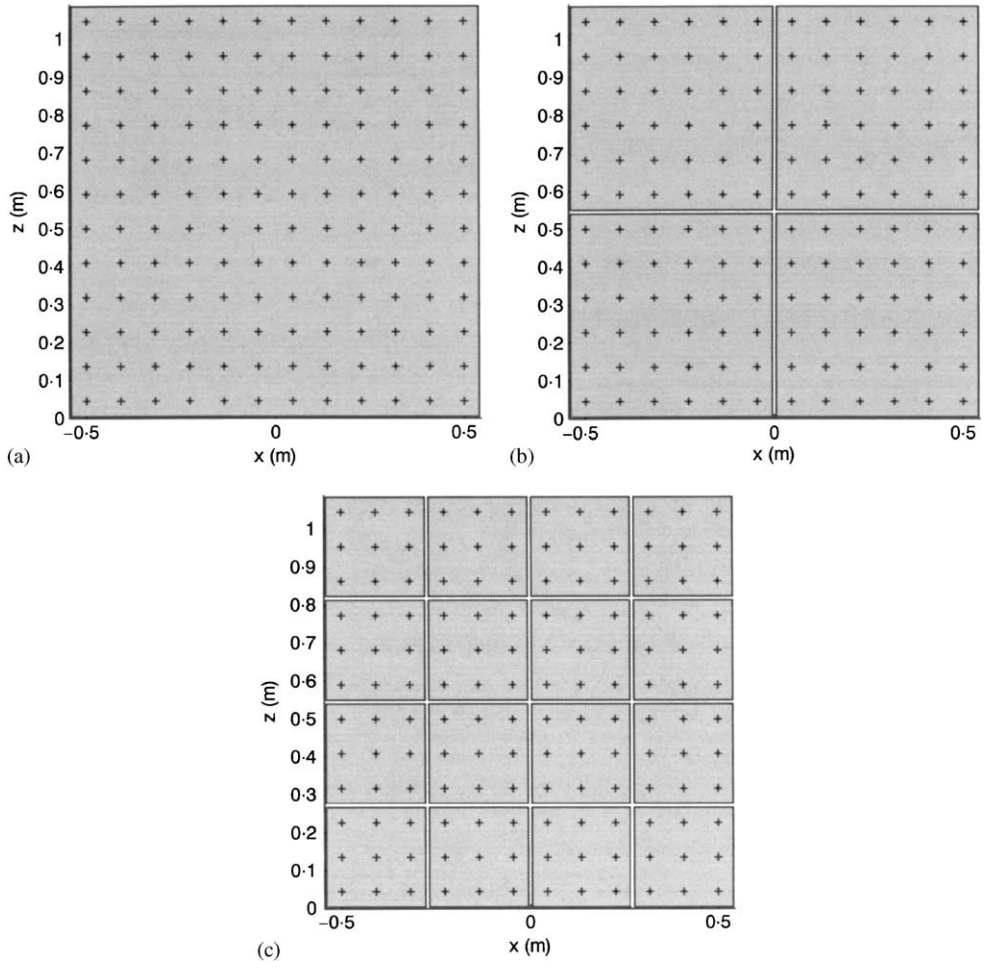

Figure 3. Square array apertures and uniform segmenting schemes. Gray regions represent subsections and the underlying grid points in each subsection are denoted by " + " symbols. The segmented array apertures shown in (a), (b), and (c) result from the application of segmenting schemes 1, 2, and 3 respectively.

microphones tend to spread evenly over the grid. Note that the theoretical model that is described in section 3 is applicable only when the number of microphones in each subsection is the same. Therefore, 3×3 subsections were not considered here (since 16- and 64-microphone arrays were considered in the present study).

The mainlobe width and peak sidelobe level of an array configuration can be estimated from the squared magnitude of its aperture smoothing function, $W(\mathbf{k})$, defined as

$$W(\mathbf{k}) = \sum_{r=1}^{M} \exp(\mathrm{j}\mathbf{k} \cdot \mathbf{x}_r). \tag{2}$$

In equation (2), $\mathbf{x}_r$ and $\mathbf{k}$ denote the rth sensor's position vector and the wave number vector respectively. Therefore, the aperture smoothing function represents the two-dimensional spatial Fourier transform of the microphones' positions.

For each array configuration generated here, the squared magnitude of the aperture smoothing function was calculated using a zero-padded (96×96)-point FFT. An example of

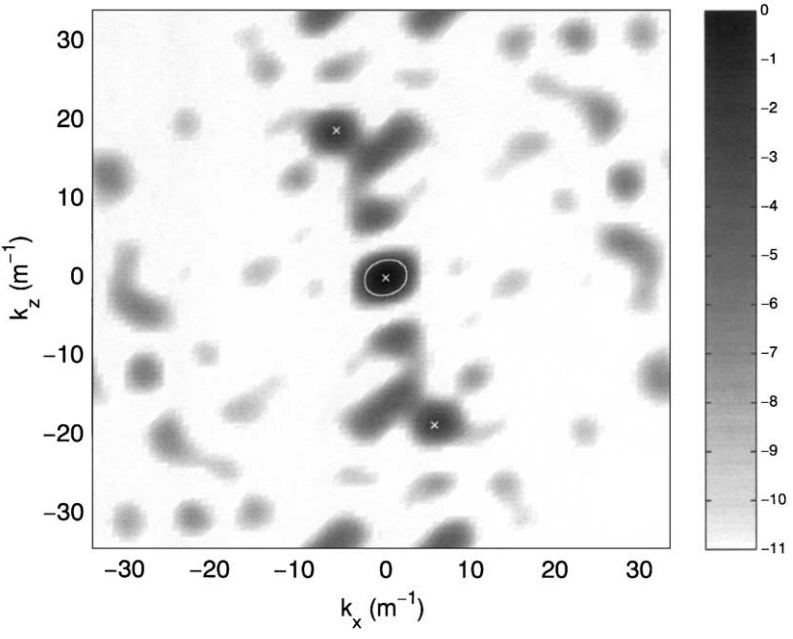

Figure 4. An example of the squared magnitude of the aperture smoothing function of an array generated using segmenting scheme 2. The x at the center of the plot represents the peak of the mainlobe and the other two x's represent the peak sidelobes. The closed curve at the mainlobe location shows the 3 dB down contour line. The scale bar represents a decibel scale.

the squared magnitude of an aperture smoothing function generated using segmenting scheme 2 for 16 microphones is shown in Figure 4. From the squared magnitude of the aperture smoothing function, the mainlobe widths based on the 3 dB down contour lines and peak sidelobe levels can be calculated and are shown in Figure 4. Note that the present work is concerned with two-dimensional array configurations and "mainlobe width" in the present article, in fact, represents the mainlobe "area" which therefore has the unit of m^{-2} (area in the wave number domain).

Two thousand, 16-microphone array configurations were randomly generated by using each of segmenting schemes 1, 2 and 3, and the 3 dB down mainlobe widths and the peak sidelobe levels in each case are plotted in Figure 5(a), 5(b) and 5(c) respectively. The best choice of an array configuration from amongst all the random arrays would be the array configuration that yielded the smallest mainlobe width and the lowest peak sidelobe level. It can be seen in Figure 5(a–c) that an appropriate choice of an array configuration is from those at the lower bound of the distributions: that is, from those arrays having the smallest possible mainlobe bandwidth for the same peak sidelobe level.

When segmenting schemes 2 and 3 are considered (2×2 and 4×4 uniform subsections respectively), it can be seen from Figure 5(b) and 5(c) that the lower bound of the mainlobe width did not change very significantly from the lower bound shown in Figure 5(a) (although the lower bound in the case of segmenting scheme 3 does seem to be somewhat higher than in the other two cases). The main effect of the segmenting is to decrease the variation of the mainlobe width distribution. The array configurations distributed within the upper portion of Figure 5(a) are presumably those array configurations that have much smaller effective aperture sizes than the nominally specified aperture size. Therefore, the introduction of uniform segmenting schemes in the generation of random arrays helps to

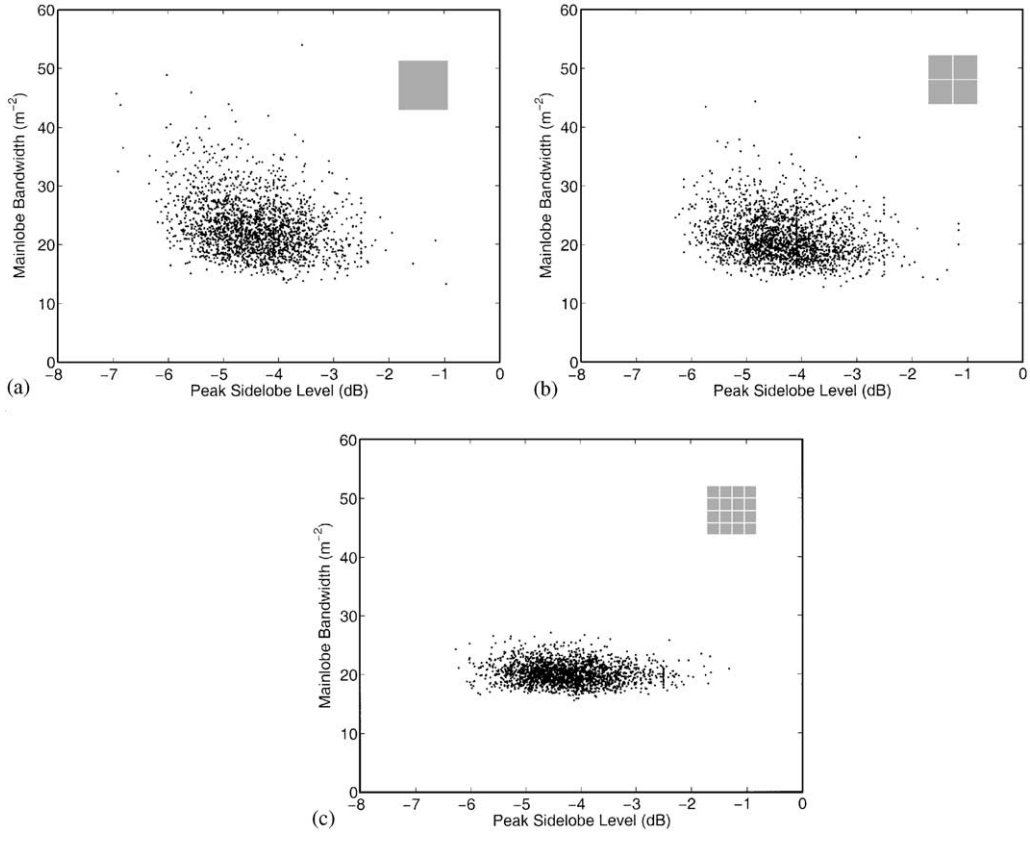

Figure 5. Correlation between the peak sidelobe levels and the 3 dB down bandwidths of sets of 2000 randomly generated arrays generated using: (a) segmenting scheme 1, (b) segmenting scheme 2, and (c) segmenting scheme 3.

filter out array configurations having relatively large mainlobe widths for the same peak sidelobe level without losing those array configurations at the lower bound. For this reason, it was decided to use the uniform 2×2 segmenting scheme in the present work (since segmenting scheme 3 may be too restrictive). The random array configurations investigated in the present study were generated based on segmenting scheme 2, unless stated otherwise.

3. THEORETICAL MODEL AND RESULTS

3.1. MEAN AND VARIANCE OF THE APERTURE SMOOTHING FUNCTION

The mean value and the variance of the squared magnitude of the aperture smoothing function for random arrays were investigated next. These quantities have been discussed in reference [10] for random arrays created without use of a segmenting scheme. In that work, sensors were assumed to be distributed over a predefined aperture without an underlying grid. Sensors were placed randomly and independently of each other without regard to the positions of previously positioned sensors. In the present study, the formulae for the mean value and the variance of the squared magnitude of the aperture smoothing function are generalized so as to make it possible to deal with cases in which segmenting schemes are used. Even though the present discussion is restricted in detail to the case of a uniform 2×2

segmenting scheme, the formulae which will be presented here can be applied to general segmenting schemes comprising any number of arbitrarily shaped subsections. The only constraint that is imposed in the derivation procedure is that the same number of sensors should be assigned to each subsection.

To simplify the following analysis, it was assumed that each sensor could be placed anywhere within each subsection without regard to the predefined grid points. The squared magnitude of the aperture smoothing function of array configurations comprising M sensors can be expressed as [10]

$$|W(\mathbf{k})|^2 = \sum_{r_1=1}^{M} \sum_{r_2=1}^{M} \exp\{\mathrm{j}\mathbf{k}\cdot(\mathbf{x}_{r_1} - \mathbf{x}_{r_2})\}, \tag{3}$$

where $\mathbf{x}_r$ and $\mathbf{k}$ denote the rth sensor's position vector and the wave number vector respectively.

The mean squared magnitude of the aperture smoothing function for random array configurations can then be expressed as

$$E[|W(\mathbf{k})|^2] = \sum_{r_1=1}^{M} \sum_{r_2=1}^{M} E[\exp\{\mathrm{j}\mathbf{k}\cdot(\mathbf{x}_{r_1} - \mathbf{x}_{r_2})\}]. \tag{4}$$

The latter summation can be divided into the two cases, $r_1 = r_2$, and $r_1 \neq r_2$: that is,

$$E[|W(\mathbf{k})|^2] = M + \sum_{r_1=1}^{M} \sum_{\substack{r_2=1 \\ r_1 \neq r_2}}^{M} E[\exp\{\mathrm{j}\mathbf{k}\cdot(\mathbf{x}_{r_1} - \mathbf{x}_{r_2})\}]. \tag{5}$$

Moreover, the $r_1 \neq r_2$ cases can be further divided into cases in which the two sensors at r_1 and r_2 lie within the same subsection and the case in which they lie within two different subsections, i.e.,

$$\begin{aligned} E[|W(\mathbf{k})|^2] = M &+ \sum_{p=1}^{n} \sum_{r_1=1}^{m} \sum_{\substack{r_2=1 \\ r_2 \neq r_1}}^{m} E[\exp\{\mathrm{j}\mathbf{k}\cdot(\mathbf{x}_{r_1 p} - \mathbf{x}_{r_2 p})\}] \\ &+ \sum_{p=1}^{n} \sum_{\substack{q=1 \\ q \neq p}}^{n} \sum_{r_1=1}^{m} \sum_{r_2=1}^{m} E[\exp\{\mathrm{j}\mathbf{k}\cdot(\mathbf{x}_{r_1 p} - \mathbf{x}_{r_2 q})\}]. \end{aligned} \tag{6}$$

In equation (6), n and m, respectively, denote the number of subsections and the number of microphones within each subsection: the latter quantity is $m = M/n$. The variables p and q are integer values denoting the index number of the subsections. The second term above corresponds to the case in which the sensors at r_1 and r_2 lie within the same subsection, while the third term corresponds to the case in which they lie within two different subsections. Since the random variables $\mathbf{x}_{r_1}$ and $\mathbf{x}_{r_2}$ are independent of each other, equation (6) can be simplified to

$$E[|W(\mathbf{k})|^2] = M + m(m-1)\sum_{p=1}^{n} \Phi_p(\mathbf{k})\Phi_p(-\mathbf{k}) + m^2 \sum_{p=1}^{n} \sum_{\substack{q=1 \\ q \neq p}}^{n} \Phi_p(\mathbf{k})\Phi_q(-k), \tag{7}$$

where $\Phi_p(\mathbf{k})$ is the characteristic function of the random variable governing sensor placement in subsection p: it is defined as $\Phi_p(\mathbf{k}) = E\lfloor \exp\{\mathrm{j}\mathbf{k}\cdot\mathbf{x}\} \rfloor$, and $\Phi_p\ (-\mathbf{k})$ denotes its complex conjugate. Equation (6) can be manipulated to yield an alternate form, i.e.,

$$E[|W(\mathbf{k})|^2] = M + m^2 \sum_{p=1}^{n} \sum_{q=1}^{n} \Phi_p(\mathbf{k})\Phi_q(-\mathbf{k}) - m\sum_{p}^{n} \Phi_p(\mathbf{k})\Phi_p(-k). \tag{8}$$

Next, the variance of the squared magnitude of the aperture smoothing function about the mean value can be obtained from the formula [10]

$$\sigma^2 = E[|W(\mathbf{k})|^4] - E[|W(\mathbf{k})|^2]^2, \tag{9}$$

where the mean value of the fourth power of the magnitude of the aperture smoothing function is

$$\mathbf{E}[|W(\mathbf{k})|^4] = \sum_{r_1=1}^{M}\sum_{r_2=1}^{M}\sum_{r_3=1}^{M}\sum_{r_4=1}^{M} E[\exp(\mathbf{j}\mathbf{k}\cdot(\mathbf{x}_{r_1} - \mathbf{x}_{r_2} + \mathbf{x}_{r_3} - \mathbf{x}_{r_4})\}]. \tag{10}$$

A similar but more tedious procedure than that used to obtain equation (8) yields an equation for the fourth power of the magnitude of the aperture smoothing function, i.e.,

$$\begin{aligned}
E[|W(\mathbf{k})|^4] = {} & M(2M-1) + 4m^2(2m-1+m(n-2)u_3)\sum_{p=1}^{n}\sum_{q=1}^{n}\Phi_p(\mathbf{k})\Phi_q(-\mathbf{k}) \\
& + 4m(m^2(n-2)(1-u_3) - mn + 1)\sum_{p=1}^{n}\Phi_p(\mathbf{k})\Phi_p(-\mathbf{k}) \\
& + 2u_3m^3\,\mathrm{Re}\left\{\sum_{p=1}^{n}\sum_{q=1}^{n}\sum_{r=1}^{n}\Phi_p(2\mathbf{k})\Phi_p(-\mathbf{k})\Phi_r(-\mathbf{k})\right\} \\
& - 4m^2(m(u_3-1)+1)\,\mathrm{Re}\left\{\sum_{p=1}^{n}\sum_{q=1}^{n}\Phi_p(2\mathbf{k})\Phi_p(-\mathbf{k})\Phi_q(-\mathbf{k})\right\} \\
& - 2m^2(m(u_3-1)+1)\,\mathrm{Re}\left\{\sum_{p=1}^{n}\sum_{q=1}^{n}\Phi_p(2\mathbf{k})\Phi_q^2(-\mathbf{k})\right\} \\
& + 4m(m^2(u_3-1)+1)\,\mathrm{Re}\left\{\sum_{p=1}^{n}\Phi_p(2\mathbf{k})\Phi_p^2(-\mathbf{k})\right\} \\
& + m^2\sum_{p=1}^{n}\sum_{q=1}^{n}\Phi_p(2\mathbf{k})\Phi_q(-2\mathbf{k}) - m\sum_{p=1}^{n}\Phi_p(2\mathbf{k})\Phi_p(-2\mathbf{k}) \\
& + u_3m^4\sum_{p=1}^{n}\sum_{q=1}^{n}\sum_{r=1}^{n}\sum_{s=1}^{n}\Phi_p(\mathbf{k})\Phi_q(-\mathbf{k})\Phi_r(\mathbf{k})\Phi_s(-\mathbf{k}) \\
& + 4m^3(m(u_3-u_4)-u_3)\sum_{p=1}^{n}\sum_{q=1}^{n}\sum_{r=1}^{n}\Phi_p(\mathbf{k})\Phi_p(-\mathbf{k})\Phi_q(\mathbf{k})\Phi_r(-\mathbf{k}) \\
& + 2m^3(m(u_3-u_4)-u_3)\,\mathrm{Re}\left\{\sum_{p=1}^{n}\sum_{q=1}^{n}\sum_{r=1}^{n}\Phi_p(\mathbf{k})\Phi_p(-\mathbf{k})\Phi_q(\mathbf{k})\Phi_r(-\mathbf{k})\right\} \\
& + 4m^2\begin{pmatrix}(m-1)(m-2)-u_4m^2\\ -3m(m(u_3-u_4)-u_3)\end{pmatrix}\mathrm{Re}\left\{\sum_{p=1}^{n}\sum_{q=1}^{n}\Phi_p(\mathbf{k})\Phi_p(-\mathbf{k})\Phi_p(\mathbf{k})\Phi_q(-\mathbf{k})\right\} \\
& + 2m^2((m-1)^2 - u_4m^2 - 2m(m(u_3-u_4)-u_3))\sum_{p=1}^{n}\sum_{q=1}^{n}\Phi_p(\mathbf{k})\Phi_p(-\mathbf{k})\Phi_q(\mathbf{k})\Phi_q(-\mathbf{k}) \\
& + m^2((m-1)^2 - u_4m^2 - 2m(m(u_3-u_4)-u_3))\sum_{p=1}^{n}\sum_{q=1}^{n}\Phi_p^2(\mathbf{k})\Phi_q^2(-\mathbf{k}) \\
& + 6m(2m^2u_3(m-1) - m^3u_4 - (m-1)(m^2-m-1))\sum_{p=1}^{n}\Phi_p^2(\mathbf{k})\Phi_p^2(-\mathbf{k})
\end{aligned} \tag{11}$$

where u_a denotes the unit step function defined as

$$u_a = \begin{cases} 1, & n \geqslant a \\ 0, & \text{otherwise.} \end{cases} \tag{12}$$

Equations (8) and (11) can be evaluated easily provided that the probability density function of the random variable (the sensor's position vector **x**, in this application) is defined for each subsection. The gray regions (i.e., the shaded areas) in Figure 3 represent the subsections. Note that the subsections include the additional area around the grid points at the edge of the array so that the shaded area in Figure 3(a) can conceptually be subdivided into small adjoining square areas, each surrounding a grid location. The average of all locations within the small square area is the grid location. Therefore, the array aperture denoted by the shaded regions represents the continuous version of the discrete array aperture in the sense that both continuous and discrete array apertures share the same aperture size. That means, for instance, that the average distance of a number of sensors from the central point of the aperture when they are randomly placed in the shaded area (not necessarily on the grid points) is equal to that of the sensors when they are randomly placed on discrete grid points within the shaded area.

In Figure 6(a) is shown the mean squared magnitude of the aperture smoothing functions of random arrays based on segmenting scheme 2 with a grid size of 12×12: a uniform

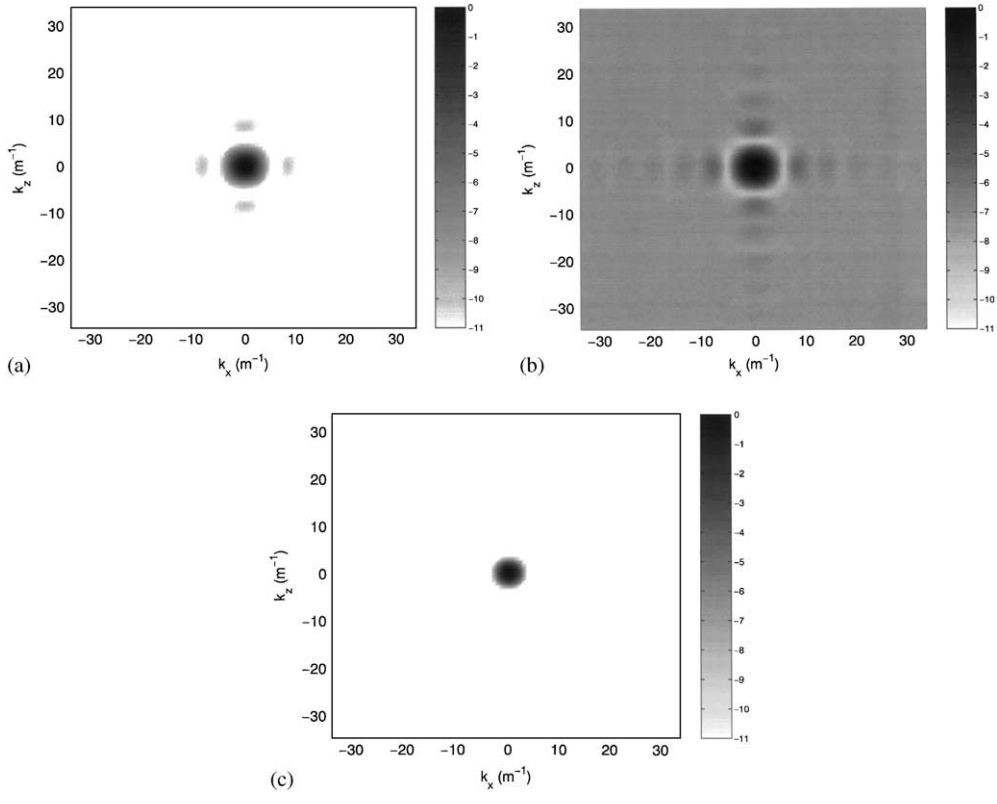

Figure 6. Mean squared magnitude of the aperture smoothing function and $\pm 2\sigma$ variations about this mean calculated for random arrays generated by using the segmenting scheme 2: (a) mean value; (b) $+2\sigma$ variation; (c) -2σ variation. Scale bar represents a decibel scale.

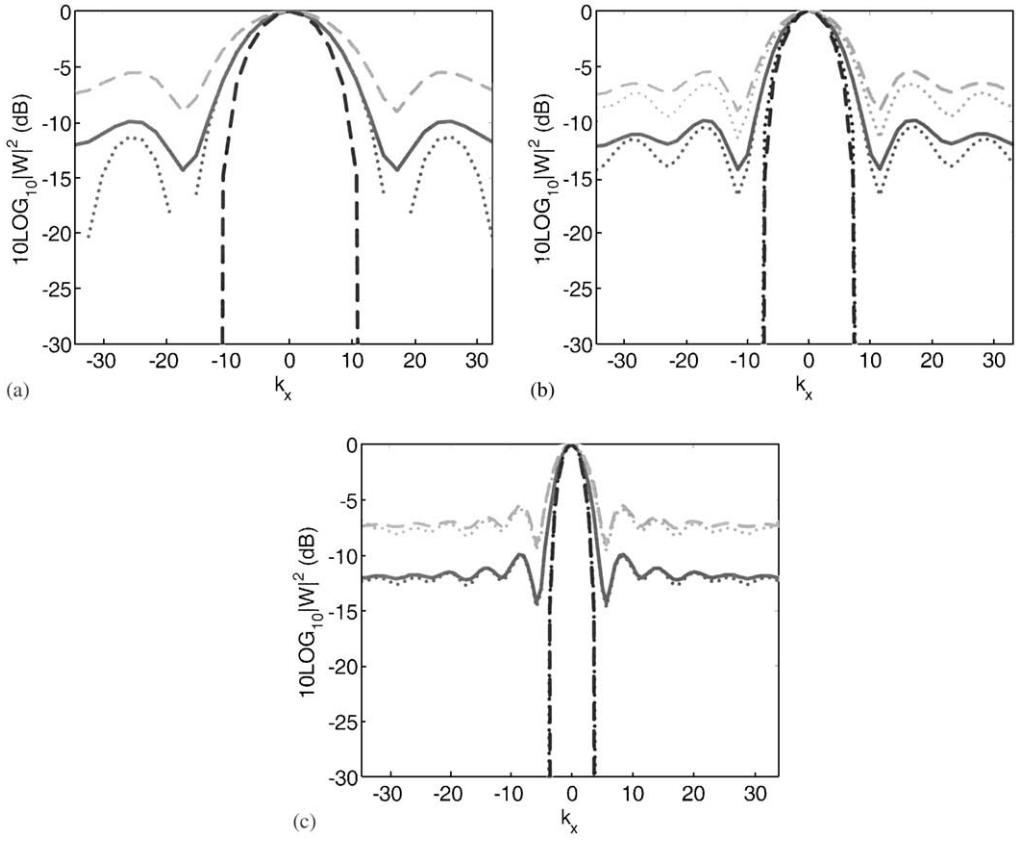

Figure 7. Cross-sections ($k_z = 0$) of the mean squared magnitude of the aperture smoothing function (solid line) and the variation ($\pm 2\sigma$) about this mean (dashed lines) calculated for random arrays generated using the segmenting scheme 2. Dotted lines denote the mean values and the variances of the squared magnitude of the aperture smoothing function, respectively, obtained by averaging results from 2000 randomly generated arrays with the same segmenting scheme: (a) 4×4 grid, (b) 6×6 grid, (c) 12×12 grid.

probability density function was assumed to apply in each subsection. In Figure 6(b) and 6(c) are shown the $\pm 2\sigma$ variations of the mean squared magnitude of the aperture smoothing functions about this mean. A cross-sectional view of Figure 6 along the line $k_z = 0$ is shown in Figure 7 along with results calculated for other sets of random arrays generated by using different grid sizes. The grid sizes used to generate the data shown in Figure 7(a), 7(b), and 7(c) were 4×4, 6×6, and 12×12 respectively. Each complete grid was divided into uniform 2×2 subsections (segmenting scheme 2), and zero-padded (32×32)-, (48×48)-, and (96×96)-point FFTs were used, respectively, to calculate the squared magnitudes of the aperture smoothing functions for 2000 randomly generated array configurations for each grid size (except for the case of a 4×4 grid, when only a single configuration is possible). In the figures, the predicted mean squared magnitude of the aperture smoothing function is denoted by a solid line, while the predicted variations ($\pm 2\sigma$) about this mean are denoted by dashed lines. The dots represent the corresponding curves calculated on the basis of the 2000 randomly generated array configurations.

It can be seen that the simulation results show progressively better agreement with the predictions of the theory as the number of grid points within a given aperture becomes

larger. This follows since equations (8) and (11) were derived based on the assumptions that sensors could be placed on the aperture continuously (i.e., without a grid), and that sensors are positioned randomly without regard to the previously positioned sensors. However, in the simulation, placing more than one microphone at the same grid point was not allowed, and sensors were positioned on discrete grid points. Therefore, the theoretical model does not account for the effects related to the number of grid points within a given aperture, and predicts identical means and variances regardless of the grid spacing so long as the aperture size is the same. However, it should be noted that the grid spacing effect exists in practice: as the grid spacing becomes smaller, the discrepancies between the predicted values and the results obtained from simulated array configurations decrease. For the case of a 6×6 grid (see Figure 7(b)), the mean value was overestimated, especially near the minima of the squared magnitude of the aperture smoothing function, by approximately 2–3 dB. Also, note that the variance tend to be overestimated compared to the actual values as the grid spacing becomes larger. For the case of a 4×4 grid, in which case, a fully populated, unique 16-microphone array configuration exists, the theory cannot predict the variance of the squared magnitude of the aperture smoothing function. Therefore, the theoretical model presented in this subsection for the mean squared magnitude of the aperture smoothing function and the corresponding variance become asymptotically exact only as the grid spacing becomes small.

3.2. MAINLOBE WIDTHS AND EFFECTIVE APERTURE SIZES

It is known that an array's mainlobe width is generally dependent on the array's aperture size. For linear arrays, the aperture size is simply the distance from one end of the array to the other. In this subsection, the relationship between the mainlobe width and the "size" of two-dimensional array configurations is investigated based on observations of random arrays generated for different segmenting schemes, grid sizes, and numbers of microphones.

There is no concrete definition of "aperture size" for two-dimensional arrays, but since aperture size in linear arrays is approximately proportional to the degree to which the microphones are spread out, it was of interest to investigate the correlation between the polar moment of an array's microphone positions and its mainlobe width (the polar moment of an array's microphone positions is defined as $\sum_{r=1}^{M} |\mathbf{x}_r|$ provided that the mass center of the array is located at the origin of the coordinate system).

In Figure 8, mainlobe widths are plotted as a function of array polar moments for five sets of 2000 random arrays generated by using the three different segmenting schemes, three different grid sizes, and two different numbers of microphones. That is, for 16-microphone arrays, the segmenting schemes 1–3 used in combination with a 12×12 grid size were tested; a different grid size, 6×6, used in combination with segmenting scheme 2, was also tested. To test a case involving a different number of microphones, 64-microphone arrays were generated by using a 24×24 grid size based on segmenting scheme 2. The grid spacing in both the x and z directions was 1/11 m for all array configurations. In Figure 8, the vertical axis represents the polar moment per sensor while the horizontal axis denotes the square root of the mainlobe width. The distributions of the polar moments per sensor (m_{ps}), and the roots of the mainlobe widths (bw_r) of the array configurations can be seen to approximately follow the curve $m_{ps} = 1{\cdot}87/bw_r$, regardless of segmenting scheme, grid size or the total numbers of sensors.

The hyperbolic relationship between the polar moment per sensor and the root of mainlobe width observed for two-dimensional arrays may be explained by analyzing linear,

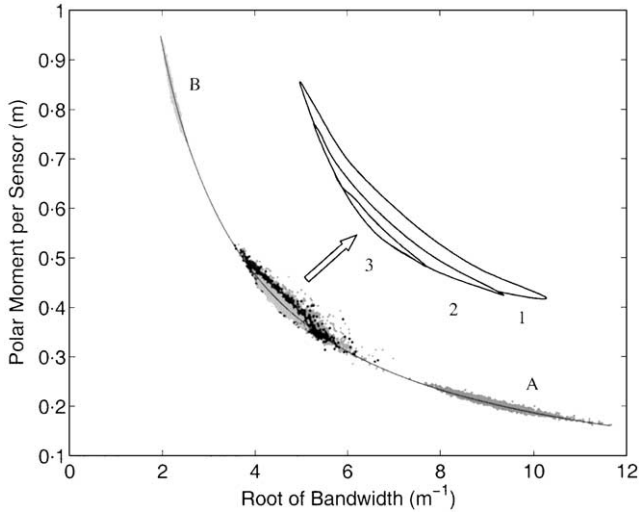

Figure 8. Correlation between the root of the mainlobe widths (bw_r) and the "polar moment per sensor", (m_{ps}), for 16-microphone random array configurations and 64-microphone array configurations. In the expanded sketch, the approximate locations of the results of the 16-microphone random arrays generated based on segmenting schemes 1, 2, and 3 and with the grid size 12×12 are denoted by 1, 2, and 3. The results for the 16-microphone random arrays based on segmenting scheme 2 with a grid size 6×6 are denoted by A. The results for 64-microphone random array configurations generated based on segmenting scheme 2 with the grid size 24×24 are denoted by B. Data points were curve-fitted (shown as a solid line) by using the formula, $m_{ps} = 1{\cdot}87/bw_r$.

regular (i.e., fully populated) arrays. Consider, a linear regular array composed of M sensors with sensor spacing, d. The mainlobe width, bw, of the linear array is [10]

$$bw = 4\pi/Md. \tag{13}$$

Here, the mainlobe width is not the 3 dB down bandwidth, but the "zero-crossing" bandwidth. The moment of the microphone positions with respect to the mass center of the array can be easily calculated, and it is $M^2\, d/4$ and $(M^2 - 1)d/4$ for even and odd values of M respectively. Therefore, the moment per sensor (with respect to the y direction provided that sensors are positioned on the x-axis) can be approximated as

$$m_{ys} = Md/4. \tag{14}$$

Note that equation (14) yields negligible error even when M is a relatively small number (for example, there is a 4 per cent error for the case $M = 5$). From equations (13) and (14), the moments per sensor can be related to the mainlobe widths for the case of linear regular arrays, i.e.,

$$m_{ys} = \pi/bw. \tag{15}$$

Note that variables M and d do not appear explicitly in equation (15).

In the case of two-dimensional regular arrays, it is reasonable to assume that the above result can be applied in both the x and z directions, independently, i.e., the moments of microphone positions about the $z = 0$ and $x = 0$ axes (provided that the mass center of an array is positioned at $z = 0$ and $x = 0$) determine the mainlobe width in the k_x and k_z directions respectively.

Note that the above procedures were derived for fully populated arrays. However, it can be seen in Figure 8 that the hyperbolic relation between the mainlobe widths and the moment per sensor still holds for sparse arrays. In Figure 8, the root of the mainlobe width,

bw_r (in fact, the root of the mainlobe "area", which has the same dimension as the mainlobe width in linear arrays) was used as the scale for the horizontal axis and instead of investigating the relationships in the x and z directions independently, the polar moment per sensor, m_{ps}, was used as the scale of the vertical axis since the apertures were square in the present case. The constant used to fit the data was 1·87, i.e.,

$$m_{ps} = 1{\cdot}87/bw_r. \tag{16}$$

This constant appears to be universal in the sense that it is independent of the grid spacing and the number of sensors.

The agreement between the data and the fitted curve seems to be good at least for the array configurations generated by using segmenting schemes that ensure a degree of "squareness" of the distributions of the microphones: small deviations from the hyperbolic relationship can be observed for some array configurations generated by using segmenting scheme 1 since the latter does not impose any restrictions on the microphone placement (note that the distributions of the polar moments of the 16-microphone random arrays generated by using a 12×12 grid based on segmenting schemes 1–3 are illustrated by means of a sketch in Figure 8). Based on the present simulations and analysis, it is also reasonable to suggest that the mainlobe widths of linear sparse arrays also depend strongly on the moment of the arrays' microphone positions, even though this dependency has not been rigorously investigated in the present study.

It was shown in reference [2] that elliptical arrays generally have smaller mainlobe widths than do random arrays even when the latter have relatively larger aperture sizes. That observation can be explained in terms of the array polar moment. Even though the nominal array aperture sizes defined by the area within the envelope of the array configurations of elliptical arrays are generally smaller than those of random arrays generated on the rectangular aperture enclosing the elliptical arrays, the corresponding polar moment of the elliptical array configurations can be larger since all of the microphones are positioned around the edges of the array envelope.

Therefore, it is concluded here that the polar moment per sensor with respect to the center of the microphone array, m_{ps}, should be used as a measure of the equivalent array aperture size in the case of square, two-dimensional arrays. In the case of non-square arrays, moments about the x- and z-axis determine the mainlobe width in the z and x directions respectively. In that case, equation (14) may be used to define the equivalent aperture dimensions of a two-dimensionally sparse array configuration. That is, based on the fact that the aperture size of a linear regular array is approximately four times the moment per sensor of the linear regular array, the equivalent aperture dimensions of a two-dimensional array configuration in the x and z directions, respectively, can be defined as four times the moments of the sensors about the z- and x-axis, respectively, i.e., $L_x = 4m_{zs}$ and $L_z = 4m_{xs}$ where L_x and L_z are the equivalent aperture dimensions in the x and z directions.

3.3. RANGE OF THE MAINLOBE WIDTH DISTRIBUTION

The formulae for the mean value and variance of the squared magnitude of the aperture smoothing function do not give direct information about the statistical properties of the mainlobe widths or the peak sidelobe levels. In the present subsection, an approximate method that can be used to predict the range of the most likely mainlobe widths (i.e., that fall with the 1–99 percent range of the cumulative distribution) will be described.

A probability density function for the distribution of the 3 dB down mainlobe widths was obtained based on 20 000, 16-microphone array configurations that were randomly

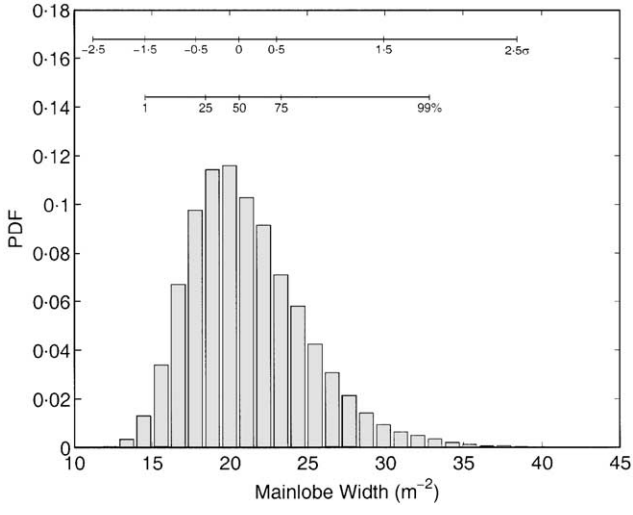

Figure 9. Bar graph of the probability density function for the distribution of the 3 dB down mainlobe widths based on 20 000 16-microphone random arrays generated using segmenting scheme 2 on a 12×12 grid size. The lower of the two horizontal lines plotted above the PDF represents the accumulated percentage of the distribution (data); the upper horizontal line denotes the mainlobe widths that were obtained from corresponding variations from the mean squared magnitude of the aperture smoothing function (theory).

generated on a square 12×12 grid using segmenting scheme 2 and a grid spacing of 1/11 m: the probability density function is shown in Figure 9 where the cumulative distribution (in two forms) is also shown above the bar graph. Note that a larger number of array configurations was used here so that the distribution as well as the mean value could be modelled more accurately. The probability density function for the distribution of the mainlobe widths was observed to be skew-symmetric. Here the object was not to identify an appropriate probability distribution model for the distribution of mainlobe widths, but to find an approximate method for predicting the range of the mainlobe widths within which fall most of the 3 dB down mainlobe widths.

As shown in Figure 7(a–c), the variance of the squared magnitude of the aperture smoothing function from the mean value is large in the sidelobe regions. However, the variance of the squared magnitude of the aperture smoothing function is small around the mainlobe (it is zero at $k_x = k_z = 0$), and therefore information about the mainlobe widths can be well estimated by using equations (8) and (11). The mean value and the plus and minus variation of the mainlobe 3 dB down (half-power) bandwidth can be obtained by contouring the mean, mean + variation, and mean − variation surfaces of the squared magnitude of the aperture smoothing function ($|A_p|^2$) at the -3 dB plane and by calculating the areas within these contours. Mainlobe widths were calculated for several settings of the variation: $\pm\sigma$, $\pm 1{\cdot}5\sigma$, and $\pm 2{\cdot}5\sigma$. The mean and standard deviation (σ) of $|A_p|^2$ as a function of the wave number were obtained by using equations (8) and (11) respectively. The 3 dB down mainlobe width resulting from these calculations are shown on the upper line in Figure 9, where the variation used to produce the result is indicated. It can be seen that the mainlobe widths that correspond to $\pm\sigma$, $\pm 1{\cdot}5\sigma$, and $\pm 2{\cdot}5\sigma$ are not positioned symmetrically with respect to the mean value of the mainlobe width ($\sigma = 0$). The asymmetry is expected from the asymmetry in the probability density function of the 3 dB down mainlobe width, which is also reflected in the large differences between Figures 6(a) and 6(b) and the relatively smaller differences between Figures 6(a) and 6(c).

The lower of the two horizontal lines above the estimated probability density function in Figure 9 represents the location of specific points in the cumulative distribution (obtained by integration of the probability density function). It can be seen that 98 per cent of the mainlobe widths lie between the values associated with the variation $-1{\cdot}5\sigma$ and a variation somewhere between $+1{\cdot}5\sigma$ and $2{\cdot}5\sigma$.

To test whether the value below which only 1 per cent of the mainlobe widths lie is well predicted by calculating the 3 dB down mainlobe width from the (mean $-1{\cdot}5\sigma$) squared aperture smoothing function for other grid sizes and other microphones, 2000 random arrays were generated for each of nine different grid sizes for the case of a 16-microphone array designed according to segmenting scheme 2 and having a grid spacing of 1/11 m. The grid sizes considered here were 4×4, 5×5, 6×6, 7×7, 8×8, 12×12, 16×16, 24×24, and 48×48. For the case of 64-microphone arrays, a further 2000 random arrays were generated in a similar manner for 10 different grid sizes: 8×8, 9×9, 10×10, 12×12, 16×16, 20×20, 24×24, 28×28, 48×48, and 72×72. Note that for the cases 5×5 and 7×7 for the 16-microphone arrays and for the 9×9 case for the 64-microphone arrays the whole grid cannot be divided evenly due to the odd numbers of grid points in the x and z directions: thus the grid was horizontally divided below the central row and vertically divided left of the central column of the grid in these cases. For each array realized in this way, a zero-padded FFT with the number of points in each direction eight times greater than the given nominal array size was used to evaluate the 3 dB down mainlobe widths. The grid sizes tested in the present work for 16- and 64-microphone arrays, respectively, are shown in Table 1 along with their interpretations in terms of, for instance, the total number of possible array configurations. In Table 1, the "best possible baselines number" represents the number of different baselines that can be formed given a number of microphones, while the "number of baselines on grid" represents the number of different baselines that can be formed given a grid. Thus the "packing ratio", defined as the best possible baselines number divided by the number of baselines on the grid, represents the degree of population of a number of microphones positioned on a grid in terms of baselines. The packing ratio of a minimum redundant array configuration would approach a value of unity.

Since the lower end of the mainlobe width distribution is of prime concern, the range of mainlobe widths associated with $\pm1{\cdot}5\sigma$ deviations were calculated for each grid size and were compared with the range of mainlobe widths within which fall 98 per cent of the mainlobe widths (i.e., 1–99 per cent in the cumulative distribution). A comparison of the ranges of half power mainlobe bandwidths obtained from the 2000 randomly generated array configurations and the predictive model for each grid size is shown in Figure 10(a) and 10(b) for 16- and 64-microphone arrays respectively. Note that the "grid size" used as the vertical axis of Figure 10 is simply the total number of the grid points (for instance, 25 in the case of a 5×5 grid). In Figure 10, the ranges of mainlobe widths obtained from the randomly generated arrays are represented by the lighter gray bars, while the range of the mainlobe widths associated with the $\pm1{\cdot}5\sigma$ deviations of the squared magnitude of the aperture smoothing functions are represented by the darker gray bars for each grid size (note that there are no light bars for the cases of 4×4 (16-microphone arrays) and 8×8 (64-microphone arrays) since only a single fully populated array configuration is allowed for those cases). The symbol $\times$ within each bar represents the mean values of the mainlobe widths.

It can be seen that the lower ends of the ranges and the mean values predicted by the theory agree very well with those obtained from the simulations for larger grid sizes for both the 16- and 64-microphone arrays. For the smaller grid sizes, the mean values of the mainlobe widths are well predicted but the variations of the mainlobe widths were overestimated by the theory. This follows since the variation of the squared magnitude of

TABLE 1

Grid sizes tested and corresponding packing ratios for each 16- *and* 64-*microphone arrays*

Number of microphones	(a) Best possible baselines (lag) numbers	Grid size	Number of possible array configurations (based on segmenting scheme 1)	(b) Number of baselines on grid	Packing ratio = **a**/**b**
16	${}_{16}C_2 + 1 = 121$	$4 \times 4 = 16$	${}_{16}C_{16} = 1$	$4 \times 4 + 3 \times 3 = 25$	4·84
		$5 \times 5 = 25$	${}_{25}C_{16} = 2\,042\,975$	$5 \times 5 + 4 \times 4 = 41$	2·95
		$6 \times 6 = 36$	${}_{36}C_{16} = 7\,307\,872\,110$	$6 \times 6 + 5 \times 5 = 61$	1·98
		$7 \times 7 = 49$	${}_{49}C_{16} = 3{\cdot}348 \times 10^{12}$	$7 \times 7 + 6 \times 6 = 85$	1·42
		$8 \times 8 = 64$	${}_{64}C_{16} = 4{\cdot}885 \times 10^{14}$	$8 \times 8 + 7 \times 7 = 113$	1·07
		$12 \times 12 = 144$	${}_{144}C_{16} = 6{\cdot}879 \times 10^{20}$	$12 \times 12 + 11 \times 11 = 265$	0·457
		$16 \times 16 = 256$	${}_{256}C_{16} = 1{\cdot}007 \times 10^{25}$	$16 \times 16 + 15 \times 15 = 481$	0·252
		$24 \times 24 = 576$	${}_{576}C_{16} = 5{\cdot}686 \times 10^{30}$	$24 \times 24 + 23 \times 23 = 1105$	0·110
		$48 \times 48 = 2304$	${}_{2304}C_{16} = 2{\cdot}860 \times 10^{40}$	$48 \times 48 + 47 \times 47 = 4513$	0·0268
64	${}_{64}C_2 + 1 = 2017$	$8 \times 8 = 64$	${}_{64}C_{64} = 1$	$8 \times 8 + 7 \times 7 = 113$	17·8
		$9 \times 9 = 81$	${}_{81}C_{64} = 1{\cdot}284 \times 10^{17}$	$9 \times 9 + 8 \times 8 = 145$	13·9
		$10 \times 10 = 100$	${}_{100}C_{64} = 1{\cdot}977 \times 10^{27}$	$10 \times 10 + 9 \times 9 = 181$	11·1
		$12 \times 12 = 144$	${}_{144}C_{64} = 6{\cdot}112 \times 10^{41}$	$12 \times 12 + 11 \times 11 = 265$	7·61
		$16 \times 16 = 256$	${}_{256}C_{64} = 1{\cdot}904 \times 10^{61}$	$16 \times 16 + 15 \times 15 = 481$	4·19
		$20 \times 20 = 400$	${}_{400}C_{64} = 1{\cdot}299 \times 10^{75}$	$20 \times 20 + 19 \times 19 = 761$	2·65
		$24 \times 24 = 576$	${}_{576}C_{64} = 9{\cdot}648 \times 10^{85}$	$24 \times 24 + 23 \times 23 = 1105$	1·83
		$28 \times 28 = 784$	${}_{784}C_{64} = 9{\cdot}652 \times 10^{94}$	$28 \times 28 + 27 \times 27 = 1513$	1·33
		$48 \times 48 = 2304$	A very large number	$48 \times 48 + 47 \times 47 = 4513$	0·447
		$72 \times 72 = 5184$	A very large number	$72 \times 72 + 71 \times 71 = 10\,225$	0·197

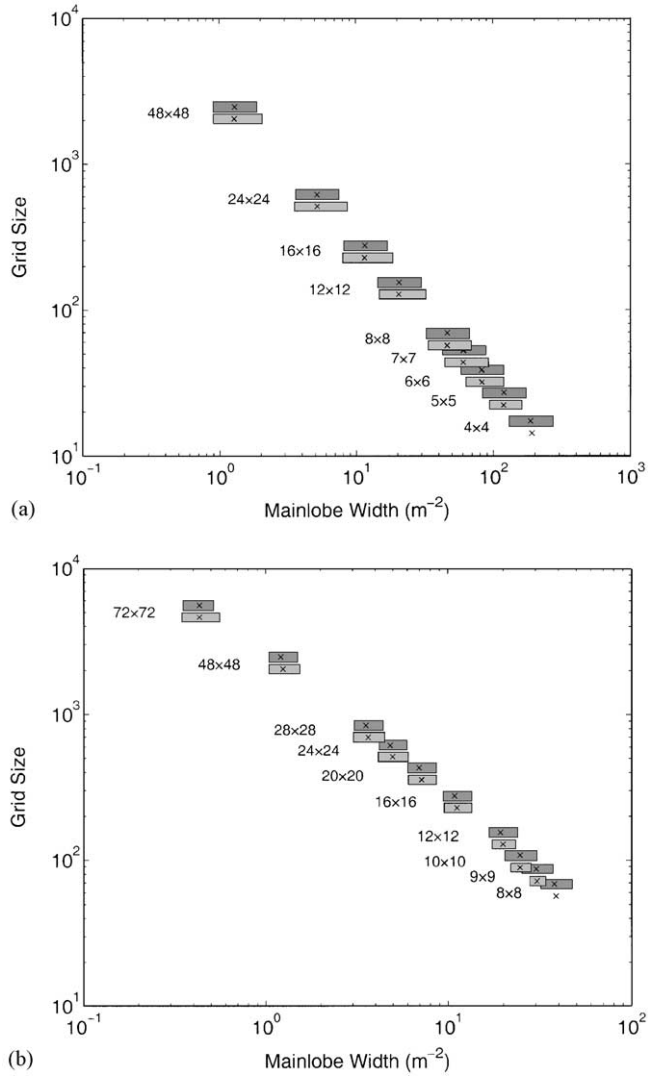

Figure 10. Comparisons between the ranges of the 1–99 per cent of distributions of 3 dB down mainlobe widths obtained from various sets of 2000 randomly generated arrays and the 3 dB down mainlobe bandwidths of the $\pm 1{\cdot}5\sigma$ variations from the mean squared magnitude of the aperture smoothing functions for different grid sizes. Each pair of bars represents the comparison for each grid size. In each pair of gray bars, the lower, lighter bar denotes the range obtained from simulated data, while the upper, darker bar denotes the range obtained from the model. In each bar, the x's represent the mean values (50% and $\sigma = 0$ respectively). (a) 16-microphone arrays; (b) 64-microphone arrays.

the aperture smoothing function is overestimated for smaller grid sizes as discussed in section 3.1. The most important conclusion to be drawn from this section, is that a mainlobe width obtained from $-1{\cdot}5\sigma$ variation of $|A_p|^2$ can be used to estimate the 1 per cent mainlobe width for the family of random arrays based on a specified array configuration. Thus, before a search of the possible random arrays begins, a grid size, grid spacing and the number of sensors can be appropriately determined according to a specified requirement on the mainlobe width.

3.4. PROBABILISTIC DISTRIBUTION OF PEAK SIDELOBE LEVELS

Next, an approximate method that can be used to estimate the mean values and the probability distribution of the peak sidelobe levels for randomly generated array configurations is presented. Equations (8) and (9) can only yield the mean values and variances of the sidelobe levels at each wave number and do not directly reveal information about the mean value and the variances of the peak sidelobe levels since the latter, in principle, can occur at all wave numbers except within the mainlobe region. The probability density function of the peak sidelobe levels depends on those functions of level distributions at each wave number in the sidelobe region. Note, however, that no information on the nature of the probability distribution function of the sidelobe levels can be obtained from equations (8) and (9).

3.4.1. *Sidelobe level probability density functions*

In the present work, the probability density function of the sidelobe level distribution was modelled based on the distribution of sidelobe levels obtained from simulations. For two locations in the wave number domain, for both 16- and 64-microphone arrays, the distributions of the sidelobe levels were obtained from 20 000 randomly generated array configurations (segmenting scheme 2, grid spacing 1/11 m). For the 16-microphone array case, the grid size used was 12×12, and the sidelobe levels were evaluated at $(k_x, k_z) = (0, -8{\cdot}64)$ and $(k_x, k_z) = (-31{\cdot}57, -31{\cdot}57)$ (refer to Figure 6 where the variance and the mean levels of the squared magnitude of the aperture smoothing function over the domain are shown). For the 64-microphone array, the grid size used was 24×24, and the sidelobe levels were evaluated at $(k_x, k_z) = (0, -4{\cdot}32)$ and $(k_x, k_z) = (-30{\cdot}21, -30{\cdot}21)$. In each case, the first of these locations is one at which the peak sidelobe occurs in the mean squared magnitude of the aperture smoothing function. The second location is that at which the sidelobe at the lower left corner in the wave number domain occurs. Figures 11(a–d) shows the probability density functions estimated from the simulations for each case. In the figures, the levels of the sidelobes are represented on a linear scale extending from zero to one where a value of one represents the normalized peak level of the mainlobe at that location.

It can be observed from the data shown in Figure 11 that the shape of the distributions are not symmetric about their mean values, and that the shapes vary depending on position in the wave number domain as well as on the number of microphones used in the array configurations. An attempt was made to curve fit the sidelobe level distributions obtained from the simulations by using conventional probability density functions. Weibull, Gamma, Exponential, and Beta density functions were tested, and the Weibull density function was found to yield the best fit with the data among the probability density functions tested. The Weibull density function is defined as [11]

$$f_X(x) = abx^{b-1}\,\mathrm{e}^{-a^x b}u(x), \tag{17}$$

where x is the random variable and $u(x)$ is the unity for $x > 0$ and zero otherwise. The two parameters in the Weibull distribution, a and b, are related to the mean, $\bar{X}$, and the variance, σ_X^2, of the random variable, x, as follows:

$$\bar{X} = \frac{\Gamma(1 + b^{-1})}{a^{1/b}}, \qquad \sigma_X^2 = \frac{\Gamma(1 + 2b^{-1}) - [\Gamma(1 + b^{-1})]^2}{a^{2/b}}, \tag{18, 19}$$

where Γ denotes the Gamma function. The two parameters a and b are uniquely related to the mean value and the variance by equations (18) and (19), while the mean values and the

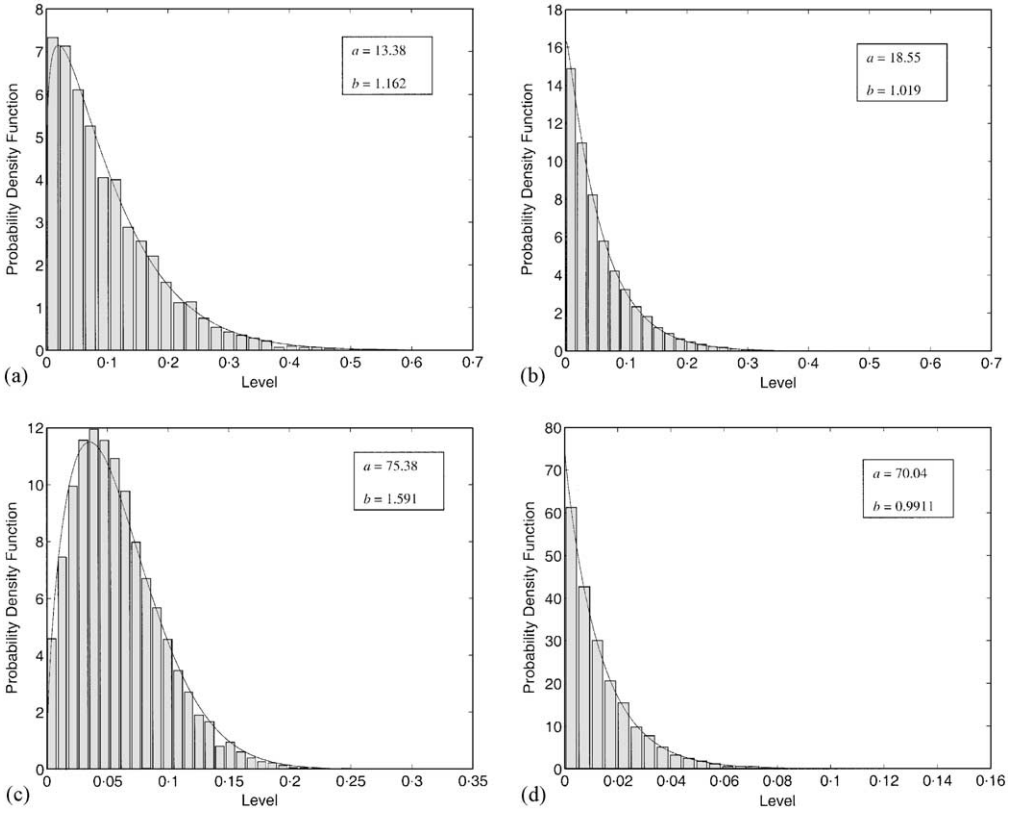

Figure 11. Plots of the probability density function for the distribution of the sidelobe levels obtained from 20 000 random arrays generated based on segmenting scheme 2. Solid lines are curves fitted based on the Weibull distribution: (a) and (b) are for 16-microphone arrays with a grid size of 12×12; (c) and (d) are for 64-microphone arrays with a grid size of 24×24. Sidelobe levels were evaluated at (a) $(k_x, k_z) = (0, -8{\cdot}64)$, (b) $(k_x, k_z) = (-31{\cdot}57, -31{\cdot}57)$, (c) $(k_x, k_z) = (0, -4{\cdot}32)$, and (d) $(k_x, k_z) = (-30{\cdot}21, -30{\cdot}21)$.

variances at arbitrary positions in the wave number domain can be obtained by evaluating equations (8) and (9). For each of the cases illustrated in Figure 11, the parameters a and b were obtained by using the method described above, and the Weibull density function fittings are represented as solid lines in Figures 11(a–d). Good agreement was found in each of the cases considered here, and so it was assumed that the distribution of sidelobe levels at each position in the wave number domain follow the Weibull distribution.

3.4.2. *Correlation of levels at two wave numbers*

Recall, however, that the distribution of peak sidelobe levels itself may not follow the Weibull distribution since the peak sidelobe does not occur at a fixed position in the wave number domain. The peak sidelobe level can be identified as the maximum level among the levels in the neighborhood of the sidelobe regions where each of the probability distributions of the level was modelled as following a Weibull distribution. In practice, the levels of the squared magnitude of the aperture smoothing function are correlated at neighboring wave numbers and uncorrelated at distant wave numbers. Lo [8] assumed that the process of determining the peak sidelobe levels could be approximated as determining

the maximum level among a finite number of independent events of random variables. The approach followed in the present study was based on the same idea.

Since the number of "independent events" through which the peak sidelobe level is determined would depend on the area in the wave number domain over which a level of the squared magnitude of the aperture smoothing function at a particular wave number has a strong influence, it is of interest to look at the correlation between levels of the function at two different wave numbers. The degree of the correlation between two random variables can be quantified by the covariance of the two random variables. The covariance is a joint moment and is defined as follows for two random variables, X and Y [10]:

$$\mathrm{cov}[X, Y] \equiv E[XY] - E[X]\,E[Y]. \tag{20}$$

The correlation coefficient is a covariance normalized with respect to the standard deviations of the random variables X and Y, i.e.,

$$\rho_{X,Y} = \frac{\mathrm{cov}[X, Y]}{\rho_X \rho_Y}, \tag{21}$$

where ρ_X and ρ_Y represent the standard deviations of the two random variables X and Y respectively.

It is perhaps possible that the correlation coefficient relating levels of the squared magnitude of the aperture smoothing function at two wave numbers, $\mathbf{k}_1$ and $\mathbf{k}_2$, can be investigated theoretically. However, the derivation of the correlation coefficient relating levels of the squared magnitude of the aperture smoothing function at two wave numbers for the case of random arrays generated based on segmenting scheme 2 would certainly be

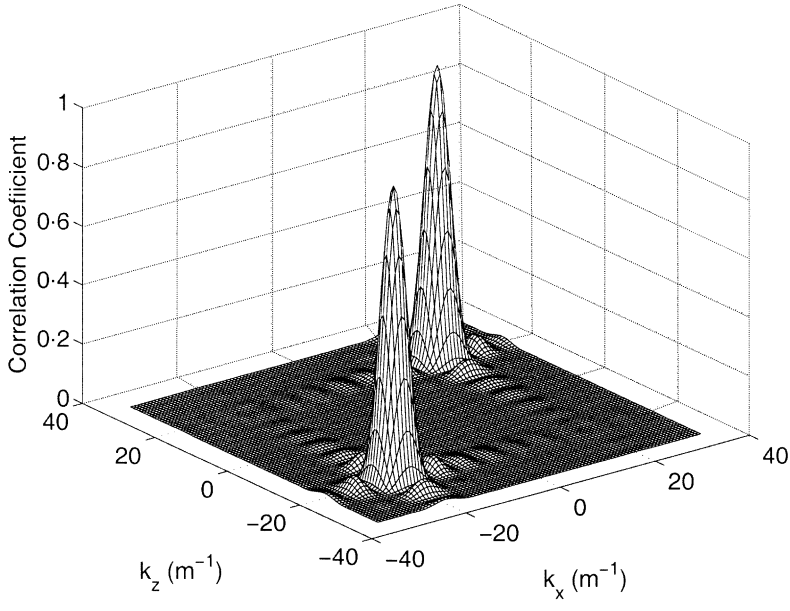

Figure 12. The correlation coefficient between the level of the squared magnitude of the aperture smoothing function evaluated at $\mathbf{k}_1 = (-20, -20)$ and levels evaluated at other wave numbers, $\mathbf{k}_2$, for 16-microphone random arrays with grid size 12×12.

a tedious task, if not actually impossible. Here, the correlation coefficient for the simpler case of segmenting scheme 1 was derived instead, and that result is

$$\rho_{X,Y} = [2(M-2)\mathrm{Re}\{\Phi(-\mathbf{k}_1)\Phi(\mathbf{k}_2)\Phi(\mathbf{k}_1-\mathbf{k}_2) + \Phi(\mathbf{k}_1)\Phi(\mathbf{k}_2)\Phi(-\mathbf{k}_1-\mathbf{k}_2)\} + |\Phi(\mathbf{k}_1+\mathbf{k}_2)|^2 + |\Phi(\mathbf{k}_1-\mathbf{k}_2)|^2 - 2(2M-3)|\Phi(\mathbf{k}_1)|^2|\Phi(\mathbf{k}_2)|^2]/$$
$$[1+|\Phi(2\mathbf{k}_1)|^2+2(M-2)|\Phi(\mathbf{k}_1)|^2+2(M-2)\mathrm{Re}\{\Phi(2\mathbf{k}_1)\Phi^2(-\mathbf{k}_1)\}-2(2M-3)|\Phi(\mathbf{k}_1)|^4]^{1/2}/$$
$$[1+|\Phi(2\mathbf{k}_2)|^2+2(M-2)|\Phi(\mathbf{k}_2)|^2+2(M-2)\mathrm{Re}\{\Phi(2\mathbf{k}_2)\Phi^2(-\mathbf{k}_2)\}-2(2M-3)|\Phi(\mathbf{k}_2)|^4]^{1/2}. \quad (22)$$

The correlation coefficient was calculated by using equation (22) for the case of 16-microphone random arrays having a grid size 12×12 and a grid spacing of 1/11 m. A plot of the correlation coefficient evaluated for a fixed $\mathbf{k}_1 = (-20, -20)$ and a varying $\mathbf{k}_2$ is shown in Figure 12. The wave number $\mathbf{k}_1$ represents one of the peak locations of sidelobes in the mean squared magnitude of the aperture smoothing function. It can be seen that the correlation coefficient decreases rapidly as the wave number $\mathbf{k}_2$ moves away from the wave number $\mathbf{k}_1$. Also note that an identical peak appears at $\mathbf{k}_2 = (20, 20)$, since the squared magnitude of the aperture smoothing function is symmetric with respect to the origin in the wave number domain. Thus the results of Figure 12 show that the levels of the squared magnitude of the aperture smoothing function are almost uncorrelated with that at $\mathbf{k}_1 = (-20, -20)$ outside the area very close to the peaks of the correlation coefficient.

Shown in Figures 13(a) and 13(b) are the 0·05-level contour lines of the correlation coefficient when $\mathbf{k}_1$ was set to the each of the sidelobes locations of the mean squared magnitude of the aperture smoothing functions: (a) for the case of a 16-microphone array with grid size 12×12; (b) for the case of a 64-microphone array with grid size 24×24 (the grid spacing in all cases was 1/11 m). In the figures, sidelobe peak locations (i.e., excluding the mirror sidelobes) are denoted by x's. For the case of the 64-microphone array shown in Figure 13(b), the central portion of the wave number domain was expanded so that it included as many sidelobe peaks in the $\mathbf{k}_x$ and $\mathbf{k}_z$ directions as in the case of the 16-microphone array. It can be found from equation (22) that the relative scales of the contour lines with respect to the spacings between the sidelobe peaks is independent of the grid size. From a comparison of Figures 13(a) and 13(b), it can also be observed that the relative scale in the sidelobe region is not very sensitive to a change in the number of microphones.

3.4.3. *Probabilistic distribution of the peak sidelobe levels*

The probability distribution function, $F_X(x)$, was then modelled based upon the above observations. If the random variable, X (representing the peak sidelobe level), is assumed to be determined by the maximum of a set of random variables, X_i, then $F_X(x)$ can be represented as the product of the probability distribution functions for the X_i's: i.e.,

$$F_X(x) = \prod_{i=1}^{ne} F_{X_i}(x), \quad (23)$$

where X_i stands for the levels of the squared magnitude of the aperture smoothing function evaluated at each of a finite set of wave numbers, and *ne* represents the number of the wave numbers. The finite set of wave numbers in the sidelobe region should be selected, in principle, so that it meets the following two conditions: each random level, X_i, evaluated at the ith wave number is independent of X_j $(i \neq j)$ evaluated at other wave numbers among

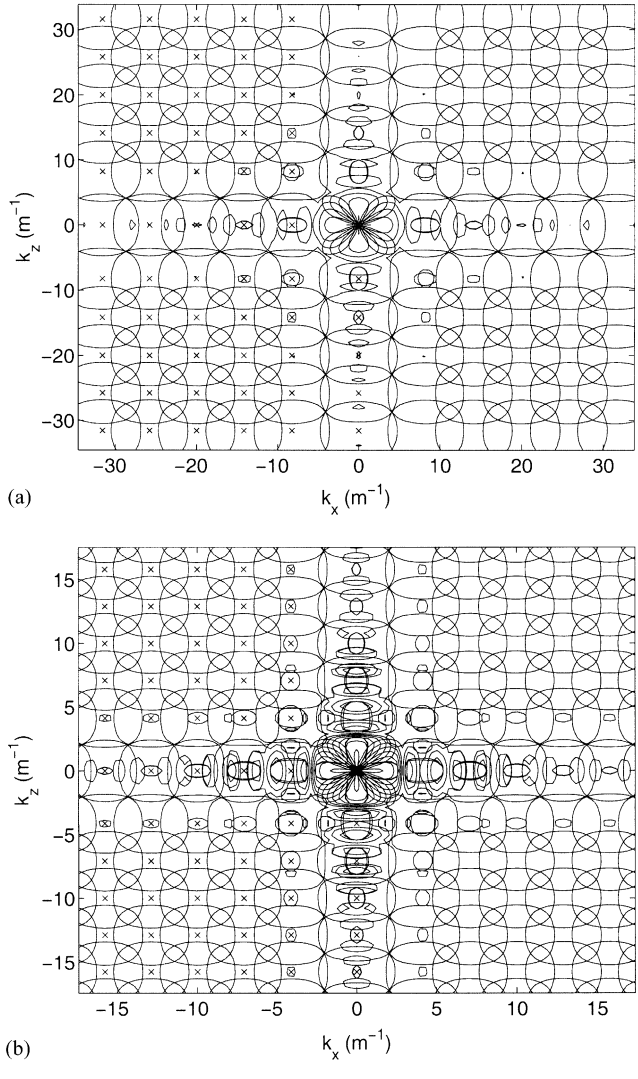

Figure 13. Contour plots for the 0·05-level correlation coefficient when the wave number, $\mathbf{k}_1$, was set to locations of sidelobe peaks in the mean squared magnitude of the aperture smoothing functions of (a) a 16-microphone array with a 12×12 grid, and (b) a 64-microphone array with a 24×24 grid.

the finite set of wave numbers, and random levels evaluated at any wave number in the sidelobe region (not necessarily in the finite set of the wave numbers) are dependent on one of the X_i's.

Such a set of wave numbers should be distributed evenly in the wave number domain of the sidelobe region since the correlation area was observed to be insensitive to change in the location in the wave number domain as shown in Figure 13(a) and 13(b). In addition, the quantity of the wave numbers to be considered (*ne*) depends linearly on the number of the whole sidelobes (*nws*), defined as

$$nws = \sum_{i=1}^{ns} w_i, \tag{24}$$

where *ns* is the number of the sidelobes and w_i is a weighting factor that depends on the appearance of the sidelobes in $|A_p|^2$: i.e., it is 1/2 for the case when only half of a sidelobe appears, 1/4 for the case when only a quarter portion of a sidelobe appears, and is unity otherwise. The weighting factor 1/2 would be assigned to the sidelobes at a boundary if an odd number of grid points in either the x or z direction were specified, while the 1/4 weighting factor would be assigned to the sidelobes at the corners if the number of grid points in both the x and z directions were odd.

Furthermore, since the area of the neighboring region over which a level has correlative influence is independent of the number of microphones (as was observed with reference to Figures 13(a) and 13(b)), the number *ne* can be assumed to be dependent only on *nws* regardless of the number of microphones used in the array configurations. The number of whole sidelobes depends on the size of the grid (the number of whole sidelobes can be seen to increase as the grid size increases as shown in Figures 7(a–c), where the number of whole sidelobes happens to be the number of sidelobes in all cases). Therefore, *ne* can be represented as

$$ne = nws \times npow, \tag{25}$$

where *npow* represents a proportionality constant that is independent of the number of microphones in the array configurations. The number, *npow*, would be unity if the correlation coefficient plots of each of the sidelobe peaks were shaped like rectangular columns of unit height and if those columns were assumed to divide the whole wave number domain, except for the mainlobe region, without overlap or gaps. However, since the plot of the correlation coefficient is cone-shaped, as shown in Figure 12, *npow* should be other than unity.

The product of *ne* probability distribution functions represented by equation (23) may be approximated by using *ns* probability distribution functions for each of the sidelobe levels at their peak locations and setting the total exponent power equal to *ne* as follows:

$$F_X(x) = \left[\prod_{i=1}^{ns} \{F_{X_i}(x)\}^{w_i} \right]^{npow}, \tag{26}$$

where X_i is the random variable that stands for the levels evaluated at the sidelobe peaks in $|A_p|^2$ (the points denoted by x's in Figures 13(a) and 13(b)). It can be seen that multiple probability distribution functions on the right-hand side of equation (23) are represented by an identical probability distribution function evaluated at one sidelobe peak if *npow* is greater than one, and a probability distribution function on the right-hand side of equation (23) is approximated by an average of probability distribution functions evaluated at multiple sidelobe peaks if *npow* is less than one.

The probability distribution function, $F_{X_i}(x)$, for the level distribution at the ith sidelobe can be obtained by integrating the probability density function given by equation (17). To estimate an appropriate value for the parameter *npow*, a few values of order unity were tested. The predicted probability density functions $f_X(x)$ which can be obtained by differentiating $F_X(x)$ in equation (26) with respect to x were compared with the probability density functions obtained from 20 000 random array configurations for the cases of 16- and 64-micrphone random arrays, respectively (12×12 and 24×24 grid sizes, respectively, segmenting scheme 2, and grid spacing 1/11 m for both cases). The results are shown in Figures 14(a) and 14(b) for 16- and 64-microphone random arrays respectively. Values of 1, 2, 3 and 4 for *npow* were used in the prediction. It can be seen that the shape of the predicted probability density function is almost independent of the change in the exponent power, and that the predicted distributions agree reasonably well with the shape of the probability density functions obtained from simulations both for 16- and 64-microphone arrays. The

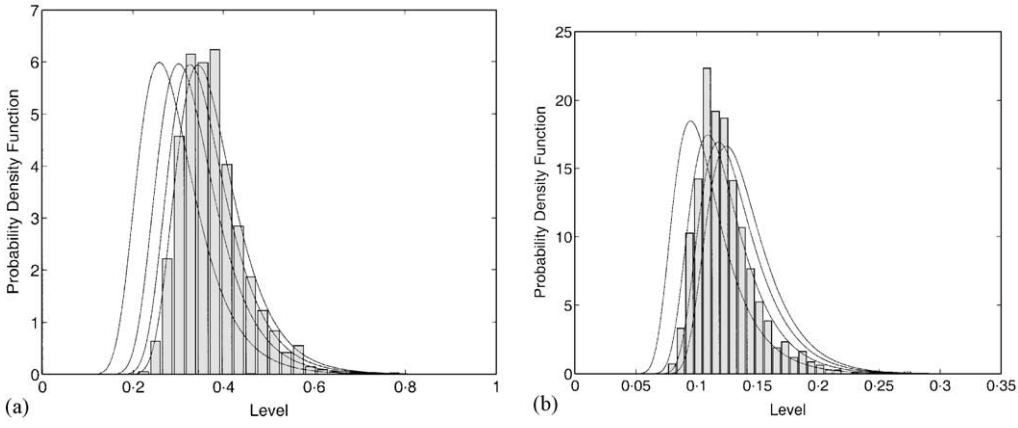

Figure 14. Probability density functions for peak sidelobe level distributions obtained from 20 000 array configurations randomly generated by using: (a) 12×12 grid and 16 microphones; (b) 24×24 grid and 64 microphones. Solid lines represent the prediction with varying the parameter, *npow*, in equation (26) from 1 to 4 (left to right).

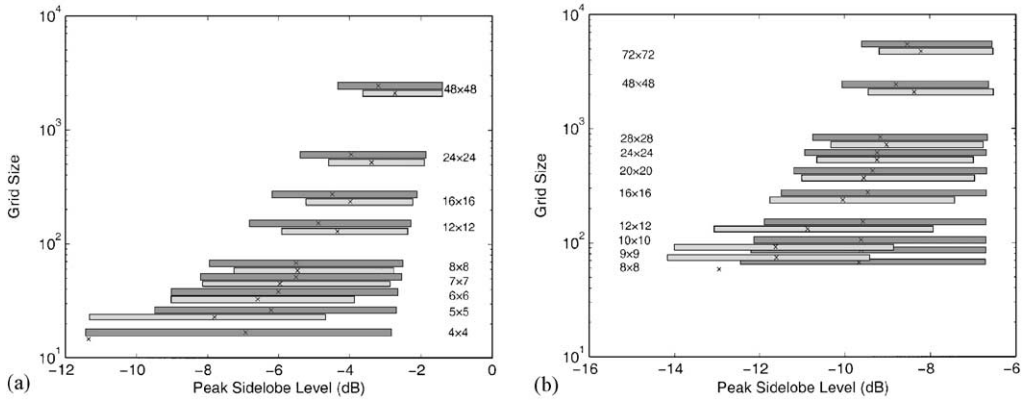

Figure 15. Comparisons between the ranges of the 1–99 per cent points of distributions of the peak sidelobe levels obtained from 2000 randomly generated arrays and those predicted by the model for different grid sizes. Each pair of bars represents the comparison for each grid size. In each case, the lower lighter bar denotes the range obtained from simulated data, while the upper darker bar denotes the range obtained from the model. In each bar, the x's represent the mean values: (a) for 16-microphone arrays and (b) for 64-microphone arrays.

predicted probability density function shifts to the right as the power, *npow*, increases, but the shift is not linearly related to the change in *npow*. For the 16-microphone case, a value of about 3·5 for *npow* yielded a reasonable agreement with the simulations, while a value of 2·0 yielded a better agreement with the simulated data for the 64-microphone case. The reason for the difference in the appropriate value of the parameter *npow* for the two cases is not apparent at present. However, fixing the parameter at a value appropriate for one case would not result in serious errors in the prediction for the other case.

In the present study, 2·0 was selected as the parameter *npow*, and the ranges of the 1–99 percent levels of the peak sidelobe level distributions (and the associated mean values) that were predicted were compared with those obtained from each set of 2000 array configurations randomly generated for the cases investigated earlier as shown in Figures 10(a) and 10(b). The results shown in Figures 15(a) and 15(b) are for the cases of 16- and

64-microphone arrays respectively. For each grid size in those figures, the range of the 1–99 per cent distributions obtained from the simulated data are shown as the lighter gray bars while the ranges predicted by using the theory are denoted by the darker gray bars. The mean values of the peak sidelobe levels are represented by x's within the bars.

For both the 16- and 64-microphone cases, the lower end of the range of the peak sidelobe levels obtained from the simulated data increases as the total number of grid points increases at a fixed grid spacing. This behavior is expected since the array becomes progressively more sparse as the aperture size increases (given a fixed number of sensors), and the model predicts this tendency with reasonable accuracy. For relatively large grid sizes (i.e., greater than or equal to 8×8 for the case of the 16-microphone array, and 16×16 for the case of 64-microphone array), the theoretical model predicted the 1 per cent and the mean levels with errors of less than 1 dB. For relatively small grid sizes, the 1 per cent and the mean levels are predicted to be larger than those values obtained from the simulations. This also follows from the fact that equations (8) and (9) overestimate the mean and variances of the squared magnitude of the aperture smoothing function for the case of smaller grid sizes.

It is interesting to note that the microphones can be configured so that an array possesses a lower peak sidelobe level than that of the corresponding fully populated array when the grid size is slightly increased from that of the corresponding fully populated array. In Figure 15(b), for the cases of the 9×9, 10×10, and 12×12 grid sizes, it can be seen that there exist array configurations that have lower peak sidelobe levels than that of the 8×8 fully populated array configuration whose peak sidelobe level is denoted by the symbol $\times$ in the figure. For the case of the 16-microphone arrays shown in Figure 15(a), a similar phenomenon was observed for the case of the 5×5 grid size where those array configurations are hidden in the non-appearing first 1 per cent of the distribution. In light of the discussion presented in section 3.2, it is likely that those nearly fully populated array configurations have smaller mainlobe widths than that of the fully populated array configuration since they have larger polar moments (see Figure 10(a) for the corresponding ranges of mainlobe widths).

3.5. SUMMARY

In section 3, approximate methods were described that make it possible to estimate the ranges of mainlobe widths and peak sidelobe levels, respectively, of randomly generated array configurations given a specified number of microphones and a grid size. In particular, the method presented here makes if possible to estimate the lower bound (i.e., where the distribution function $= 0{\cdot}01$) of the population of possible mainlobe widths without modelling the probability distribution function of the latter since the mainlobe widths of random arrays do not vary much from their mean value. In contrast, to estimate the range of peak sidelobe levels, it was necessary to model the probability distribution function of the peak sidelobe levels since the variance of the latter is in general large. In any particular instance, the grid size and the number of microphones can be optimized by using the predictive tools presented here to obtain random array configurations that meet the requirements for the mainlobe width and the peak sidelobe level before starting a computationally time-consuming search procedure.

For example, given a frequency range of interest, equation (1) can be used to estimate the maximum allowable grid spacing. Given a requirement for a certain mainlobe width, equation (9) in combination with equations (8) and (11) can be used to estimate the *minimum* aperture size required. Then given a requirement for a specified peak sidelobe level,

equation (26) can be used (the Weibull parameters a and b at each sidelobe peak being calculated from equations (18) and (19)) to estimate the minimum number of microphones required, or to estimate the *maximum* aperture size allowed. If application of the mainlobe width and peak sidelobe level criteria do not result in an intersection of aperture sizes, then the number of microphones should be increased. Simulations that can be used to calculate the range of the mainlobe widths and the peak sidelobe levels of the random array configurations for various grid sizes (provided that the number of microphones is fixed) should then be repeated until both the specified peak sidelobe level and the mainlobe width requirements are met. Equation (16) may be used to estimate the initial grid size to test in the simulations. If the simulations indicate that the number of microphones is too small to meet both requirements, simulations should be run for different numbers (i.e., an increased number) of microphones while fixing the grid size at that which meets the mainlobe width specification.

4. CONCLUSION

In the present work, a model was developed to predict the statistical properties of two-dimensionally sparse arrays in which a number of microphones are randomly positioned on a given grid. It was found that the model could be used to predict the range of mainlobe widths and the probability distribution of the peak sidelobe levels with reasonable accuracy for the cases of the grid sizes and the number of microphones tested here. For relatively small grid sizes compared with the given number of microphones, the effects of grid size were not negligible and the predictions deviated from the simulated data. To improve the accuracy of the predictions for the case of smaller grid sizes, exact formulae should be derived for the mean and variance of the squared magnitude of the aperture smoothing function of random arrays whose microphones are, in practice, discretely positioned (while not allowing more than one microphone to be positioned at one point).

From the simulated random array configurations generated based on different grid sizes for two different numbers of microphones, it was observed that the mainlobe width of an array configuration is inversely proportional to the average polar moment of microphone position about the mass center of the array configuration. Also, it was observed that array configurations with peak sidelobe levels lower than that of the fully populated array configuration can be obtained by randomly generating array configurations on a grid size that is slightly increased from that of the fully populated array.

ACKNOWLEDGMENTS

The authors gratefully acknowledge the financial support of Isuzu Motors Ltd. (contract monitor: Dr Hiroshi Takata).

REFERENCES

1. H. KOOK, G. B. MOEBS, P. DAVIES and J. S. BOLTON 2000 *Journal of Sound and Vibration* **233**, 137–156. An efficient procedure for visualizing the sound field radiated by vehicles during standardized passby tests.
2. H. KOOK, P. DAVIES and J. S. BOLTON 1999 *SAE Paper* 1999-01-1742, *Proceedings of the* 1999 *Noise and Vibration Conference*. The design and evaluation of microphone arrays for the visualization of noise sources on moving vehicles.
3. A. T. MOFFET 1968 *IEEE Transactions on Antennas and Propagation* **16**, 172–175. Minimum-redundancy linear arrays.

4. E. PANAYIRCI and W.-L. CHEN 1995 *Signal Processing* **42**, 319–334. Minimum redundancy array structure for interference cancellation.
5. E. VERTATSCHITSCH and S. HAYKIN 1986 *Proceedings of the IEEE* **74**, 217. Nonredundant arrays.
6. W. K. KLEMPERER 1973 *Proceedings of the IEE Conference on Radar-Present and Future*, Conference Publication, Vol. 105, 74–80. Non-redundant phased array radar.
7. S. BRÜHL and K.-P. SCHMITZ 1993 *Proceedings of INTERNOISE* 93, 1311–1314. Noise source localization on highspeed trains using different array types.
8. Y. T. LO 1964 *IEEE Transactions on Antennas and Propagation* **AP-12**, 257–268. A mathematical theory of antenna arrays with randomly spaced elements.
9. G. B. MOEBS 1997 *MSME Thesis*, *School of Mechanical Engineering*, *Purdue University*. De-Dopplerization and visualization of sound fields emitted by moving noise sources.
10. D. H. JOHNSON and D. E. DUDGEON 1993 *Array Signal Processing-Concepts and Techniques*. Englewood Cliffs, NJ: Prentice-Hall.
11. Z. PEYTON and J. R. PEEBLES 1987 *Probability*, *Random Variables*, *and Random Signal Principles*. New York: McGraw-Hill; second edition.